# The Initial Stage of Uranium Oxidation: Mechanism of UO<sub>2</sub> Scale Formation in the Presence of a Native Lateral Stress Field

Z. Chernia,\*,† Y. Ben-Eliyahu,† G. Kimmel,‡ G. Braun,† and J. Sariel†

Nuclear Research Center-Negev, P.O. Box 9001, Beer-Sheva 84190, Israel, and Institutes for Applied Research, BGU, P.O. Box 653, Beer-Sheva 84105, Israel

Received: May 8, 2006; In Final Form: August 25, 2006

In this work, an oxidation model for α-uranium is presented. It describes the internally lateral stress field built in the oxide scale during the reaction. The thickness of the elastic, stress-preserving oxide  $(UO_{2+x})$  scale is less than 0.5  $\mu$ m. A lateral, 6.5 GPa stress field has been calculated from strains derived from line shifts  $(\Delta(2\theta))$  as measured by the X-ray diffraction of UO<sub>2</sub>. It is shown that in the elastic growth domain, (110) is the main UO<sub>2</sub> growth plane for gas-solid oxidation. The diffusion-limited oxidation mechanism discussed here is based on the known "2:2:2" cluster theory which describes the mechanism of fluorite-based hyperstoichiometric oxides. In this study, it is adapted to describe oxygen—anion hopping. Anion hopping toward the oxide-metal interface proceeds at high rates in the  $\langle 110 \rangle$  direction, hence making this pipeline route the principal growth direction in UO<sub>2</sub> formation. It is further argued that growth in the pure elastic domain of the oxide scale should be attributed entirely to anion hopping in  $\langle 110 \rangle$ . Anions, diffusing isotropically via grain boundaries and cracks, are shown to have a significant impact on the overall oxidation rate in relatively thick ( $>0.35 \mu m$ ) oxide scales if followed by an avalanche break off in the postelastic regime. Stress affects oxidation in the elastic domain by controlling the hopping rate directly. In the postelastic regime, stress weakens hopping, indirectly, by enhancing isotropic diffusion. Surface roughness presents an additional hindering factor for the anion hopping. In comparison to anisotropic hopping, diffusion of isotropic hopping has a lower activation energy barrier. Therefore, a relatively stronger impact at lower temperatures due to isotropic diffusion is displayed.

# Introduction

Uranium surface oxidation by  $O_2$ /water vapor, while studied comprehensively in recent years,  $^{1-7}$  still presents a notable challenge. Uranium shows a variety of oxidation states, of which the +4 state is most favored.  $^{4,8-11}$  Correspondingly, the uranium dioxide lattice is formed, presenting a CaF<sub>2</sub>-type ionic structure of an  $O^5_h$  space group with one U and two O atoms for a unit cell.  $^{12,13}$  Gradually, the stoichiometry of the oxide scale built upon a metal increases  $^{2,4,6}$  at the air—oxide interface due to oxygen diffusion  $^{14}$  confinements. Eventually,  $UO_2$  transforms through  $UO_{2+x}$  (0 < x < 0.25) to  $U_4O_9$  and (when a higher, +5 oxidation state of uranium is formed to balance additional anion negative charge  $^{15,16}$ ) to  $U_3O_8^{1,4,11}$  (at temperatures elevated beyond 250 °C).

Defect clustering in fluorite crystals was extensively discussed in the past.  $^{15,17-26}$  Evidence for anion clustering in doped fluorites was found in ESR and ENDOR studies by Bleaney et al.  $^{17}$  and Baker et al.  $^{20}$  A basic superlattice cell named as the '2:2:2-cluster<sup>27</sup> contains six Bravais fluorite lattices. In doped CaF<sub>2</sub> (Cheetham et al.  $^{21}$ ) and other fluorites such as the  $UO_{2+x}$  (Willis  $^{18,19,24}$ ), it accommodates two types of anion interstitials, both distorted from cube center position and vacancies at regular anion sites. The superlattice ordering was later discussed by Catlow and Lidiard.  $^{15,22,23}$  For the hyperstoichiometric  $UO_2$ , it was shown  $^{26}$  that the growth in the oxide content is instigated by additional interstitial oxygen anions, introduced at specific

locations along the  $\langle 110 \rangle$  crystal direction. Up to two such sites are populated in a single cluster. Their formation is accompanied by a slight shift in the positions of two other oxygen anions in the superlattice cluster, along the  $\langle 111 \rangle$  line. Consequently, the high symmetry of the UO $_2$  lattice is degraded, as its structure gradually takes on an orthorhombic deviation, following anion addition and reposition.

For up to 10-nm-thick oxide scale, the oxidation process follows logarithmic-type time dependency, well described by Mott—Cabrera. <sup>28,29</sup> According to this mechanism, the flow of O<sup>2-</sup> anions toward the reacting metal—oxide interface is driven by Coulumbic force caused by the electric potential built across the oxide film. The reduction of the electric potential instigated by the oxide scale growth decreases the Mott—Cabrera mechanism contribution to the oxidation. In the following step, other rate-controlling mechanisms become significant and affect the overall reaction kinetics.

At temperatures higher than 100 °C, diffusion-limited parabolicrate kinetics governs the oxidation reaction up to a point, wherein the escalating elastic stresses between the oxide scale and the metal substrate cracks the surface of the oxide. Finally, the disruption in the diffusion-limited regime transforms the oxidation rate into a "paralinear" dependency,<sup>30–32</sup> followed by the "spallation" of the outer surface. Yet, this "classic", oversimplified type of behavior is very much dependent on the specifics of sample preparation and on the exact environmental conditions applied. Surface issues such as roughness, often not appreciated, may facilitate evolution of the process directly into paralinear or even linear stages. Moreover, the oxidation kinetics is highly sensitive to the presence of the environmental humidity

<sup>\*</sup> Corresponding author. E-mail: chernia1@netvision.net.il.

<sup>†</sup> Nuclear Research Center-Negev.

<sup>‡</sup> Institutes for Applied Research.

even at parts per million scale concentrations. In cases where water molecules are participating in oxidation process, oxidation kinetics is enhanced dramatically while presenting complex, hydrogen-associated oxide formations.  $^{2,3,31,33}$  Multiple oxide-phase evolvement through the UO $_2 \rightarrow$  UO $_{2+x}$ , U $_4$ O $_9$ , and U $_3$ O $_8$  path, known to take place in most oxidation conditions, presents an additional difficulty in a precise description of uranium corrosion.

Though much is known on various kinetic rates of polycrystalline uranium oxidation at different stages and at diverse environmental conditions, some basic features of parabolic growth dynamics of the cubic UO2, essential in a precise understanding of oxidation of uranium, have not been adequately described. In essence, the present work intends to bridge the gap between the theoretical works on 2:2:2 clustering of Willis<sup>18,19,24</sup> and Allen et al.<sup>25,26</sup> and the kinetic studies of the dynamic growth behavior of the oxide. 23,31-34 For this goal, diffusion-limited oxidation has to be viewed on the basis of the 2:2:2 cluster description and account for the presence of a native stress field. The stress field is mounted during the elastic, precracking stage of the oxidation process, as the continuous oxide surface coverage grows out from the much denser uranium. Hence, while unable to dissipate laterally, a crystal stress field with the main compressive element resting in the lateral plane is expected to rise at nonequilibrium. Another kind of anisotropic behavior, to be called "structural anisotropy", is likely to be formed due to a more favorable embedment of some crystallographic planes of the dioxide, in the uranium polycrystalline matrix. The resulting anisotropic tendency is revealed in a preferential oxidation of those planes and may be readily monitored by X-ray diffraction. These are the principal phenomena which we were interested in finding in this work. Namely: (1) deriving a quantitative description of the stress field, (2) finding a qualitative description for the mechanism, which shall account for the structural anisotropy and for the preferential oxide growth, and (3) depicting the alterations in oxidation rates and oxide-growth dynamics, imposed by the evolving anisotropic stress field, which is expected to mount during uranium oxidation.

In the present work, fine polished samples of  $\alpha$ -U were oxidized in dry air or dry oxygen at 120–160 °C. In the diffusion-controlled stage, a thin film of UO<sub>2</sub> with a very low but theoretically inevitable hyperstoichiometric fraction developed on a metal surface. Since we have limited our work to the precracking stages of the oxide film growth, the thickness would not extend beyond the elastic stress range. Therefore, the oxidation of the metal was confined to the formation of thin oxide scale of  $\leq$ 0.5  $\mu$ m thickness.

X-ray diffraction (XRD) was the main method used here to measure structural and stress anisotropies. The stress anisotropy may be deduced in a way similar to the one practiced in the analysis of Cr<sub>2</sub>O<sub>3</sub> scale, built upon Ni-25Cr bulk in O<sub>2</sub> atmosphere at high temperature.<sup>35</sup> Our newly developed reflectance-based FTIR technique was utilized for in situ monitoring of the scale buildup in its elastic and plastic growth regions (including an in situ pinpointing of the beginning of oxide cracking).

## **Experimental Section**

**Sample Preparations.** Samples of rolled, stressless<sup>36</sup>  $\alpha$ -U of approximately 1 cm<sup>2</sup>  $\times$  0.2 cm each underwent fine mechanical polishing with 1- $\mu$ m diamond paste and were then cleaned in an ultrasonic bath and oxidized in dry, dynamically held (100 cm<sup>3</sup>/min) air or an UHP O<sub>2</sub> atmosphere for 1.0–12

h at 160-120 °C, respectively. Samples were oxidized until 0.15-0.50- $\mu$ m-thick oxide film was formed. The oxidation was processed in Harrick's reaction chamber ("Refractor Reactor"), mounted into our IR spectrometer, thus enabling an in situ measurement of the oxide scale thickness escalation. Temperature monitoring was performed by a thermocouple pressed against the sample. An even, nonlocalized oxidation in Harrick's reaction chamber was obtained upon shutting down water cooling. Prior to heating, the reaction chamber containing the uranium sample was purged by a stream of dry  $O_2$  or  $N_2$  for several hours to eliminate residual moisture. The oxidizing atmosphere presented  $\sim 5-10$  ppm humidity at the reactor entrance. After the desired oxide thickness was reached, the samples were X-rayed, revealing a highly oriented dioxide layer on top of a nonperfect  $\alpha$ -U.

IR Reflectance and X-ray-Diffraction Setup. A Harrickproduced grazing angle Refractor Reactor equipped with a pair of ZnSe-wedged windows had been coupled to a wire grid on a KRS-5 substrate polarizer manufactured by SPECAC. This enabled us to examine S-polarized reflectance in situ in order to monitor the oxidation rate of the reaction. Our Bruker Equinox-55, research-grade FTIR spectrometer was utilized in a wide NIR-MIR spectral range (10000-380 cm<sup>-1</sup>), which enabled an interference reflectance pattern detection starting from 0.1  $\mu$ m film thickness (see details of this method in the following section). A DTGS/KBR detector with a KBR beam splitter for NIR-MIR was utilized. A Spectra-Tech IR-Plan Advanced Cassegrain optics-based microscope, equipped with an MCT liquid-N2-cooled detector and 15×-Reflachromat wideangle objective, had been attached to the side port of our Bruker spectrometer. While operated in reflection mode, it allowed us to examine distinctive spectral features of cracked vs precracked surface spots of the oxide.

X-ray diffraction measurements were executed with a Philips PW-3020 diffractometer, while  $\theta$  and  $2\theta$  were coupled. A power supply of 40 kV, 40 mA, and a Cu anode ( $\lambda = 1.54056$  Å) with a Ni filter were used. The detector was a proportional Xe detector with a graphite monochromator located in the front of the unit. The scan range was normally  $2\theta = 20-90^{\circ}$ .

## **Oxidation Monitoring Method**

Before discussing the oxidation process, we present here our method for monitoring oxide scale thickness mounted upon a metal surface. In general, light, specularly reflected from the upper surface of a smooth dielectric scale, interferes with its phase-delayed refracted-light element reflected from the lower scale. This phase delay is proportional to the dielectric properties of the scale, frequency of the incident light, angle of incidence, and thickness of the film. The effect of altered phase difference in growing UO<sub>2</sub> scale for the S-polarized light is demonstrated in a set of FTIR spectra presented in Figure 1. These spectra were taken at constant time periods during the oxidation of  $\alpha$ -uranium in dry air at 160 °C until 260-nm-thick oxide was obtained. The interference modes presented in Figure 1 are named after Fuchs and Kliewers<sup>37,38</sup> (FK). They were treated as "virtual" (the modes were described as strong-type interacting polaritons and were postulated to only emit, not to absorb, photons), radiative solutions for incoming/outgoing oscillating polarized waves in a thin film.<sup>37–40</sup> In the case of the dielectric scale on top of a perfect reflecting metal substrate, those polaritons are separated into pairs of orthogonal, tangentcotangent solutions, characterized by their mutually exclusive polarizations. The FK formalism can be utilized (by applying numerical methods) to describe a single absorbing stoichiometric

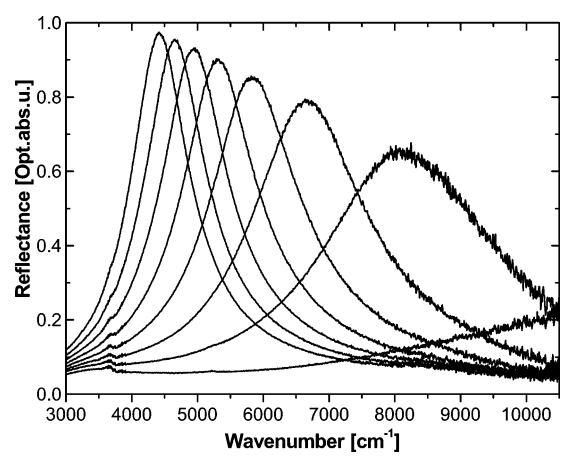


**Figure 1.**  $\alpha$ -U oxidation at 160 °C in dry air, as monitored by S-polarized reflectance. Oxidation was maintained until an overall 0.26- $\mu$ m-scale thickness was attained. Successive plots are presented with 5-min intervals, as they are red-shifted. The 38-min monitoring was initiated at a high-frequency peak, indicative of a  $\sim$ 0.13- $\mu$ m-thick scale.

dioxide scale developed on top of an ideal polycrystalline metallic surface (a nonideal case is also applicable). Since the oxide scale is nonstoichiometric and has a complex structure, a better theoretical approach is needed. Here it is assumed that the oxide scale is made of two sublayers. The upper layer is pure  $UO_2$ , whereas the lower 60-nm-thick scale presents an interface at the uranium boundary. It embodies the dioxide with an admixture of uranium metal ( $\sim 30\%$  volume fraction). Assuming such structure, Fresnel equations to model IR reflectance from the surface (see Appendix A for calculation details) were utilized. This enabled us to derive the  $UO_2$  scale thickness.

Detailed discussion on other model setups is beyond the scope of this work and will be presented elsewhere. For now, it is pointed out that the introduced model scheme has a solid grounding in Auger-surface profiling with very good optimization features in terms of scale thickness calculations. While a superior alternative would have an additional element of a stress-driven anisotropy, introduced in a two-element dielectric tensor, the presented scheme served its purpose remarkably well, with a better than 5% error margin in oxide thickness estimation.

#### **Results and Discussion**

A. Main XRD Features of Anisotropic Oxide Scale. Figure 2 presents a diffractogram taken from a sample of α-U oxidized in dry O2 at 160 °C. FTIR reflectance measurement reveals 0.27μm-thick dioxide scale. The UO<sub>2</sub> was identified as a fluorite cubic structure. The four reflections 111, 200, 220, and 311 are given. In the following discussion those are named A, B, C, and D, respectively. Exact peak positions were deduced by assigning a proper calibration error (due to a possible misalignments of  $2\theta$ ), which was derived from a Rietvield fit. We note that since the overall line-shift fit of UO<sub>2</sub> was not adequate, <sup>41</sup> the Rietvield algorithm was utilized for peaks of the U-substrate alone. The realigned UO<sub>2</sub> line shifts were then derived manually. The expected diffraction lines from published data<sup>42-44</sup> are marked. The α-U substrate is marked by six diffraction lines<sup>45</sup> (see the dashed lines markings in Figure 2). Although the  $\alpha$ -U  $2\theta$  positions match exactly, the intensities proportion implies a rather-preferred orientation—a feature which is clearly attributed to the rolled origin of the samples (a possible influence of such a preferred orientation on the oxidation dynamics is argued in the next chapter). Three main distinctive features of UO<sub>2</sub> lines are readily observed:

- (I) While the 111, 200, and 311 reflections approximately follow the alleged intensities proportion (see markings of published intensities), the 220 reflection is stronger than expected by at least an order of magnitude.
- (II) There is a nonuniform shift in positions of  $UO_2$  diffraction lines toward larger than supposed diffraction angles. The smallest shift of 0.1° (in  $2\theta$ ) is for the 200 reflection, and the largest shift of 0.45° (in  $2\theta$ ) is for the 220 diffraction line.
- (III) Peaks attributed to the oxide-scattering planes are very wide, indicating nanometric grain size and a possible microstrain.

We first discuss features I and II. Three main possibilities underlie the overall tendency to negative shifts in the XRD peaks of the dioxide. The first includes negative deviation in stoichiometry which is equivalent to a larger *a*-spacing of the oxide unit cell. The second is attributed to the surface effect of very small grains which effectively enlarges the unit cell size at the air—oxide boundary<sup>46</sup> (in ceria,<sup>47,48</sup> this effect produces negative shifts when grain-size diameter is below 13 nm). The third accounts for the macroscopic stress field mounted in a lateral plane, thus creating a positive strain perpendicular to the surface.

There are major doubts in analyzing the shifts in accord with the foremost argument. First, as already pointed out, the gradual U diffusion-limited hyperstoichiometric oxidation starts from the stoichiometric UO<sub>2</sub>. Clearly, no hypostoichiometric structures of  $UO_{2-x}$  (x is the degree of hypostoichiometry) are known. Evidently, the degrading oxygen content at the metal-oxide interface deduced from the Auger depth profiling conducted in this work (see also in SIMS depth profiling of ref 2) is not caused by hypostoichiometry of UO<sub>2</sub> but by a partial oxidation of the metal grains. This is in full agreement with the common theory on oxide growth.<sup>29</sup> Moreover, even if XRD shifts from published *hyper*stoichiometric structures<sup>49–51</sup> are to be extrapolated in a positive x direction, the approximated x > 0.25hypostoichiometry (as for the "C"-plane shift) is beyond any feasible guess. In addition, there are different shifts for different planes, which have yet to be explained. Furthermore, large hypostoichiometric deviation ( $x \le 0.25$ ) should initiate sizable structural changes that would display an additional set of peaks in XRD spectra which were also absent. Indeed, the set of predefined experimental conditions utilized for U-samples oxidation ensures that the oxygen concentration gradient across the oxide film is minimal. XPS measurements combined with Auger profiling of 0.27- $\mu$ m-scale oxide built upon bulk were obtained to detect species other than U<sup>4+</sup> cations; none were found.

The second possible explanation, involving small-grain surface effect, was tested by measuring X-ray diffraction from very fine and unstrained uranium dioxide powder. The XRD spectrum presented us with a perfect dioxide structure but rather with very broad peaks. The grain size of L (in nanometers) of the powder is calculated from the width  $-\beta_T \equiv \beta_T(2\theta)$  of the diffraction peaks at half their maxima (in radians):  $L = 0.9\lambda/[\beta_T \cos(\theta)]$ . For the applied X-ray source of  $\lambda = 0.154$  nm, the size of the grains was estimated as  $\sim L = 6$  nm. Those are much smaller than the grain size derived for the oxide film. Since no shifts were observed, this alternative was also excluded.

Contrary to the first two possibilities mentioned above, the lateral-stress hypothesis is well supported by the combined background evidence and can be theoretically justified. In a nonequilibrium case, where loosely packed oxide evolves out of a much denser metal matrix, a stress field with some compressive element resting parallel to the surface may be anticipated. In general, its size is a matter of structural

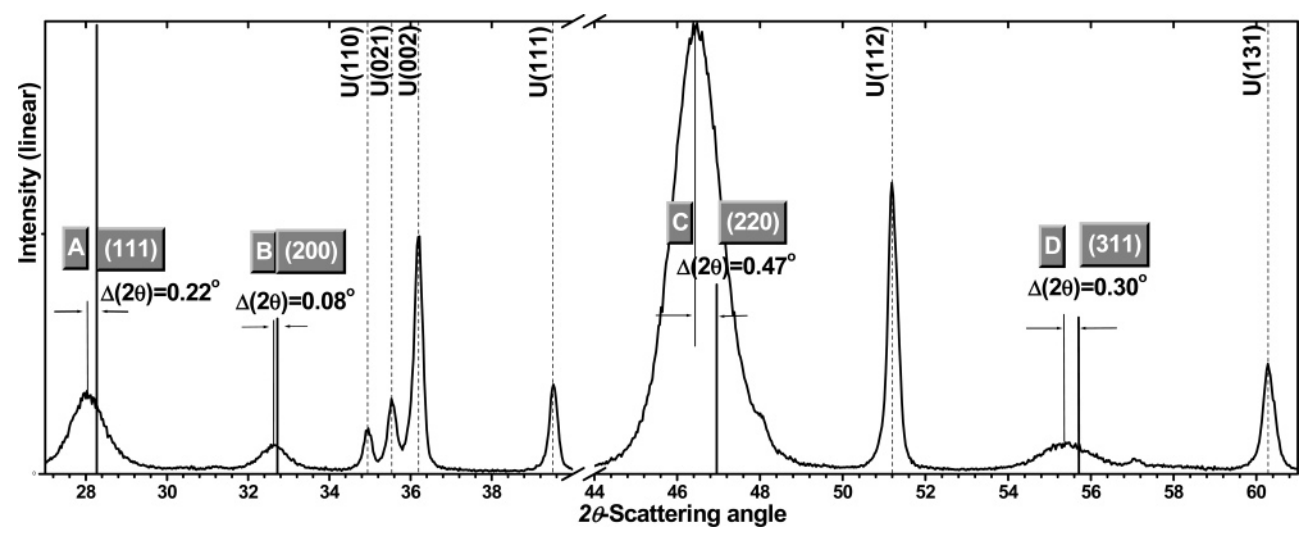


Figure 2. XRD pattern for the four main oxide scattering planes of 270 nm dioxide scale (oxidation at 160 °C in dry air atmosphere). Bold and thin perpendicular lines indicate the supposed and the actual line positions of reference UO<sub>2</sub> and of the oxide scale formed in this experiment, respectively. Conveniently,  $2\theta$  shifts are given. Heights of bold lines represent the expected relative intensity of lines in reference oxide. Six sharp scatterings are attributed to bulk α-U. Noticeably, the measured lines position match the expected reference α-U lines (dashed lines).

crystallinity (single-crystal vs polycrystalline media), matching characteristics between the oxide and the metal unit cells (mechanism which controls the width of the stress-dissipating metal—oxide interface) and the temperature gradient during the cooling phase.

It must be pointed out that the uranium matrix utilized for this work is composed of  $\sim 20$ - $\mu$ m-size polycrystallites, each divided by numerous subgrains. In such a diverse medium, the initial overall formation rate of the preferential (220) oxide is a weighted sum of the growth rates of UO<sub>2</sub> crystallites, grown upon the most reactive and abundant uranium planes. It is implied that those are the densest uranium planes, like the (023);(113) and (002). A preferred oxide plane could be shaped when the two shortest bonds of newly formed U-O are crosslinked. In the case of  $UO_2$ , those are pairs of U-O in the  $\langle 111 \rangle$ , joined together to allow (220) formation. As a result, the oxide (220) initial growth over  $\alpha$ -U is facilitated. The total preferred oxidation rate is mostly governed by the kinetics enhancement factors during the diffusion-limited regime oxidation, which is discussed in next chapters. Hence, the (110) vector is the principal growth direction of the oxide. The strong X-ray scattering from this plane originates from crystallites growing at  $\langle 110 \rangle$  normal to the surface plane. All other diffraction planes observed are mostly the projections of (220) when growing nonperpendicular to a surface plane direction, into the perpendicular one. This is visualized in Figure 3 (for the case of the

The broad line profile of XRD peaks, which is referred to as phenomenon III (see above), is usually explained as a small-grain size (GS) effect, and here also ascribed to a strong microscopic strain (MS), experienced by most of the scattering planes. The Williamson–Hall equation<sup>52,53</sup> given in eq 1 ( $\Delta\epsilon$ , microstrain; L, grain size), has been utilized to derive the GS and MS by line regression for four of the scattering planes (Figure 4).

$$\beta_{\rm T}\cos(\theta) = 4\Delta\epsilon \sin(\theta) + 0.9\lambda/L \tag{1}$$

Thus we have a GS of 18 nm and MS = 0.72% (it is noted that the line profiling tool, which accounts for a secondary Cu– $K\alpha_2$  emission at 1.54439 Å of the X-ray source, was applied here in order to assign the correct line width to the peaks in

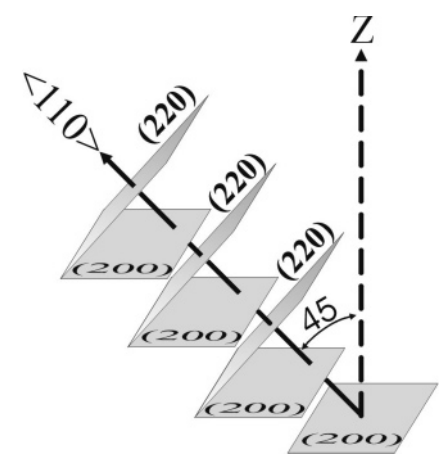


**Figure 3.** Projection of the  $\langle 110 \rangle$ , growing in a nonperpendicular (to the surface) direction. The projected (200) of the tilted  $\langle 110 \rangle$  is presented (*Z* vector points perpendicularly).

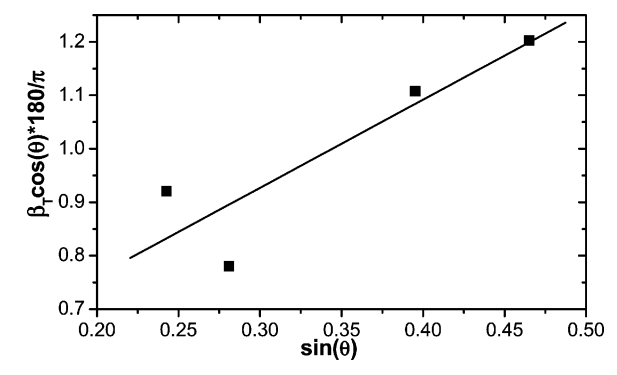


**Figure 4.** Implementation of the Williamson—Hall equation to derive (by linear regression in accord with 1') GS and MS. Here utilized for an adhesive 270-nm- thick UO<sub>2</sub> scale.

eq 1). Evidently, the high data diversity (R = 0.89) displayed in Figure 4 is due to some variations (although not accounted for) in shear stress microenvironment, experienced by different planes.

**B.** Anisotropic Stress Field. The resultant growth stress should be viewed as originating mainly from greater uranium intraatomic distances in the cubic dioxide than in the orthorhombic  $\alpha$ -U. Indeed, the shortest near-neighbor distances in the

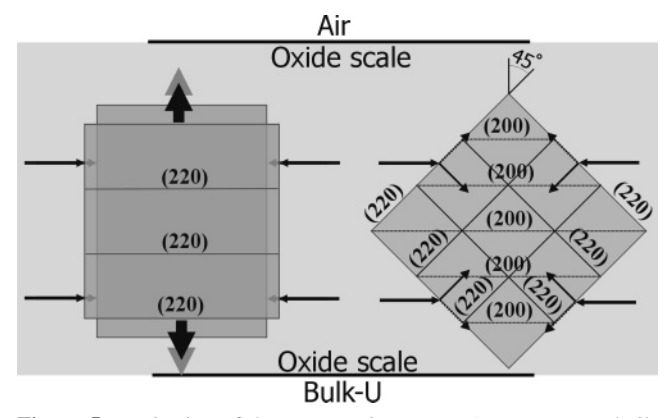


**Figure 5.** Projection of the compressing stress. A stress vector built at upright angles to the  $\langle 110 \rangle$  is projected into itself for the lateral (220) (figure at left) and into a (200) for tilted (220) (figure at right).

uranium matrix are 2.8500, 3.3285, 3.2627, and 2.7695 Å. Since the shortest U-U distance in the dioxide matrix is 3.8679 Å, the foremost oxide layers ought to be highly compressed, as they proceed to grow outward. Yet obviously, the oxide formation is not a straightforward introduction of O<sup>2-</sup> into the preexisting U matrix. Rather, it can be viewed as a newly shaped structure, occupying a much larger space by extending itself out. Presumably, as randomly oriented UO<sub>2</sub> grains grow, they are compressed at an upright angle of the respective growth direction. Yet, since growth stresses are allowed to dissipate into the main growth path outward, it is generally assumed that the stress field is accumulated and preserved in a lateral plane. Furthermore, the enhancing factor of oxidation kinetics had to be considered. From dynamic growth considerations, which are presented in the following section, all the nonperpendicular (to the surface plane) (110) growth directions are kinetically decayed. Hence, the buildup of the directional macroscopic stress field is an outcome of noncoherent microscopic stresses convolved with preferential growth dynamics. Consequently, this should accelerate the buildup of the macroscopic stress field into the lateral plane. Gradually, lateral stress accumulates up to a crashing level. Grain faces, oriented at a nonnormal incidence to such a macroscopic lateral stress field, are exposed to a strong shear stress. However, they are introduced to a much lower degree of lateral strain than their perpendicularly oriented counterpart. This is shown in Figure 5, where a cubic oxide grain tilted at 45° (rightmost figure) presents an isotropic inplane (of the page) compression at its four faces (alongside the accompanying strong shear stress elements resting across the cube faces). The remaining two faces, which are pointing outof-plane of the page, are compressed by a stronger (by 1/cos-(45°)) normal stress. In the opposite case (leftmost figure), a lateral stress field exerts strong negative strain upon a perpendicularly oriented cube and even stronger positive strain at the lateral face. Clearly, with respect to the perpendicular orientation, a straightforward application of Hook's law for a tilted cube displays an almost vanishing strain in its lateral (200)

For the perpendicularly oriented grain, for which lateral stress inflicts negative lateral strain and positive strain at upright angle, the Possion's ratio  $\nu$  is given by:

$$\nu = -\epsilon_{zz}/(\epsilon_{xx} + \epsilon_{yy}) \tag{2}$$

Strain is defined by  $(d-d_0)/d_0$ , where d is the respective measured intraplanar spacing and  $d_0$  is its strainless counterpart. Because  $\epsilon_{zz}$  is normal to lateral, it is readily derived from peak

TABLE 1: Strain Map at Different Directions<sup>a</sup>

plane indices	interplanar angle (deg)	$2\theta$ shift (deg)	derived strain normal/lateral (%)
2,2,0	0	0.47	+0.93; -1.45
3,1,1	<b>31</b> ; 65; 90	0.30	+0.50; -0.78
1,1,1	<b>35</b> ; 90	0.22	+0.76; -1.19
2,0,0	<b>45</b> ; 90	0.08	+0.25; -0.39

<sup>a</sup> The derived normal/lateral strain is proportional to the inclination angle indicated in bold font in the second row. Other inclination angles derived from indices combinations of a negligible probability growth are shown beside. The probability weight of such an inclination angle depends on the multiplicity per each plane group and the probability of the oxide to grow at a specific direction (the probability is relatively small for higher angles and it is 0% for all 90° inclinations plane groups).

shifts relative to standard UO<sub>2</sub>. Noting that for UO<sub>2</sub>,  $\nu = 0.32$  (ref 51) and lateral strain is isotropic in x' and y' ( $\epsilon_{xx} = \epsilon_{yy}$ ); therefore  $\epsilon_{zz} = -0.64 \epsilon_{xx}$ . Hence, for the perfectly normal to the surface "C"-plane case, the measured  $\Delta(2\theta) = 0.45^{\circ}$  shift (see Figure 5) imposes  $\epsilon_{zz} = 0.94\%$  in perpendicular and a huge  $\epsilon_{xx} = -1.47\%$  in lateral directions. Then for UO<sub>2</sub> known stiffness constants<sup>55</sup> ( $C_{11} = 396$  GPa;  $C_{12} = 121$  GPa) the lateral stress  $\sigma_{xx}$  is readily derived from Hook's law in accord with:

$$\sigma_{xx} = (C_{11} + C_{12})\epsilon_{xx} + C_{12}\epsilon_{zz}$$
 (3)

This results in a compressing lateral stress  $\sigma_{xx} = -6.46$  GPa. The difference in thermal expansion coefficients ( $\Delta\alpha$ ) between the oxide and the uranium was also counted as one of the obvious potential reasons<sup>35</sup> for the derived *lateral* strain. However, its size given by  $\Delta\alpha\Delta T$  provided us with only 5% of the strain estimated by XRD (for known<sup>56,57</sup>  $\alpha_{\rm U}$  and  $\alpha_{{\rm UO}_2}$ ,  $\alpha_{\rm U}\Delta T$  and  $\alpha_{{\rm UO}_2}\Delta T$  are 0.167% and 0.095 %, respectively).

Following these arguments, "C" projections on the "A";"B" and "D" planes would display a diminished degree of positive strain shift. Hence, the interplanar angle  $\phi$  between (220) and its three projections ((111);(311);(200)), calculated in eq 4, are expected to follow a strong correlation with the measured shift in  $2\theta$ .

$$\cos(\phi) = \frac{h_1 h_2 + k_1 k_2 + l_1 l_2}{\sqrt{h_1^2 + k_1^2 + l_1^2} \sqrt{h_2^2 + k_2^2 + l_2^2}}$$
(4)

Table 1 presents the derived negative (lateral) and the respective positive (normal) shifts in the last column. The second column denotes the possible interplanar angles for all Miller indices combinations. For example, X-ray 200 reflection is produced not only by (200) but also by the other scattering planes of (002) and (020). The three resulting inclinations with the (220) are divided between 45° and 90° angles. However, there is an additional consideration to be accounted, as at higher inclination angles there is a much lower growth probability (in the following section it is shown that inclination of  $\langle 110 \rangle$  in a nonperpendicular to lateral direction reduces the resultant anion flow rate at the metal-oxide interface). Consequently, for all 90° inclined planes, there is a 0% growth probability. This should effectively set all three discussed planes of Table 1 in the proper order with respect to their weighted inclination (in fact, since (111) and (200) have a single non-90° inclination, only the (311) has to be weighted). Conveniently, at 45° inclination, the strain is minimal.

It should be emphasized, that although only directional oxidation paths (perpendicular vs nonperpendicular to lateral) have been considered, there is substantial contribution to

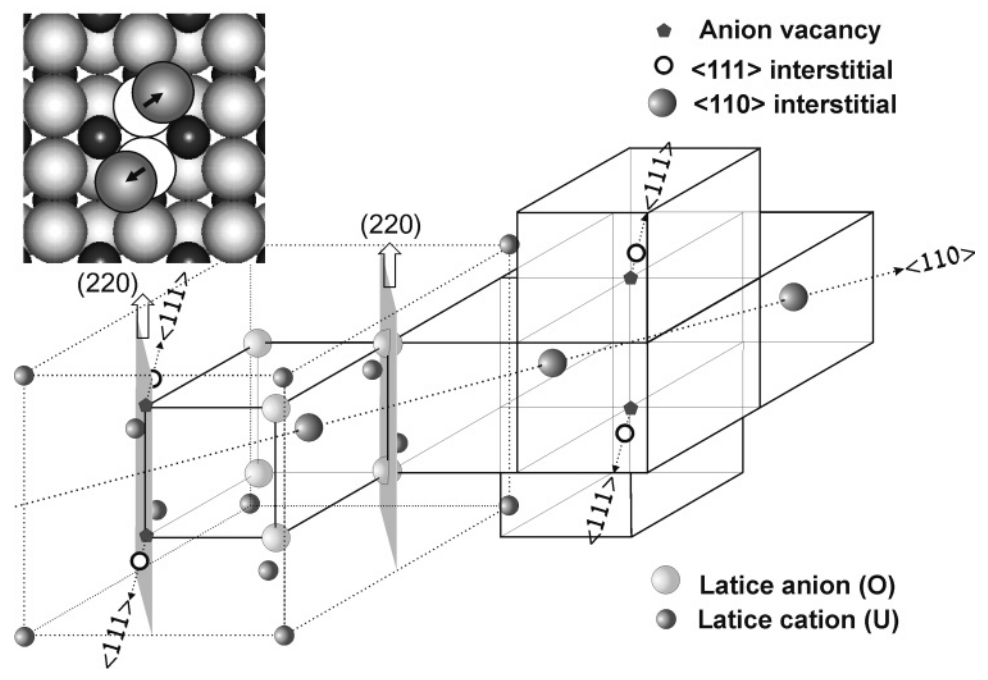
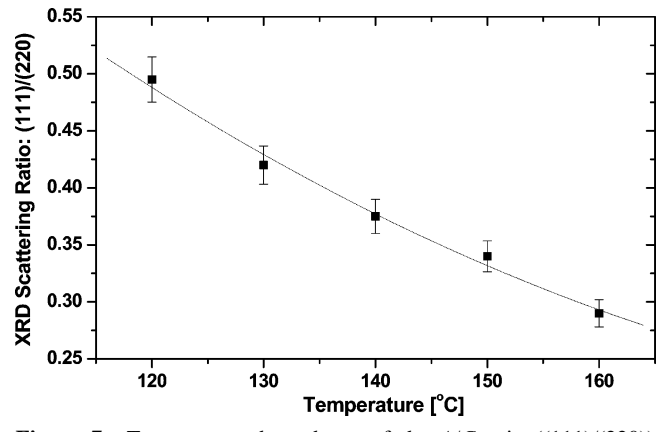


Figure 6. The 2:2:2 anion cluster. A scheme of a superlattice made of six anion cells (at the right) is presented. Anion interstitials directed along the  $\langle 110 \rangle$  are marked as dark large spheres. The two anion vacancies are marked as small pentagons, and two additional anion interstitials are indicated by small hollow circles. At the left, a figure of fluorite lattice with eight  $O^{2-}$  anions (large, bright-gray spheres) and four  $U^{4+}$  cations (small, dark spheres) at the face-centered cubic sites is shown. In the cluster oxide, the (220) is modified to include two 111-type interstitials (dark circles) shifted by  $\sim 1$  Å from their original location (white circle along the  $\langle 111 \rangle$  route). A modified (220) is visualized in the inset at the upper-left corner ( $O^{2-}$  is represented by a gray sphere;  $U^{4+}$  is shown as a smaller black sphere).

oxidation growth presented in the X-ray scattering from different, nondirectional, isotropic, anion diffusion paths.

C. Growth Dynamics. The (220) is one of the most accommodating planes in UO<sub>2</sub>. In an early work of Willis, <sup>18,19</sup> later extended by Allen et al., <sup>25,26</sup> it was suggested that the 2:2:2 clustering (see Figure 6) in hyperstoichiometric UO<sub>2</sub> proceeds via  $\langle 110 \rangle$  routes by promoting anion hopping. Two types of interstitial anions were proposed: one displaced by 0.851 Å from the empty interstice at the center of a fluorite-type cube into the  $\langle 110 \rangle$  and another displaced by 1.042 Å into the  $\langle 111 \rangle$ . We assume that the latter facilitates anion hopping by providing an accessible path in  $\langle 110 \rangle$ , as can be seen in Figure 6 (inset in the upper left corner). Evidently, the ordering of the 2:2:2 clusters follows the interstitial paths of the first type.

Initial preferred orientation buildup of the oxide planes depends on the structural properties of the α-U substrate. However, their directional buildup, perpendicular to the surface plane growth, is a kinetically controlled process. We suggest that this preferred orientation is built due to a more efficient O<sup>2-</sup> anion diffusion through the perpendicular routes than via other diffusion paths (grain boundaries, defects, dislocations, and hindered, nonperpendicular (110) routes). Accordingly, it is assumed here that anions arrived at the reaction zone through regular diffusion paths would form oxide crystallites in coincidental orientations. Consequently, the XRD spectral pattern originating in anion isotropic diffusion is expected to follow the familiar, well-documented XRD peaks intensity distribution observed in UO2 powders. Hence, the intensity of the diffraction lines (except for (220) intensity) can be exploited to quantify the efficiency of oxidation through regular diffusion paths. To compare between the two reactions paths, the intensity ratio between the diffraction lines (111) and (220) is utilized. The two XRD lines represent an extensive isotropic and directional oxidation, respectively. This ratio, denoted as the "A/C" ratio,



**Figure 7.** Temperature dependence of the A/C-ratio ((111)/(220)) derived for samples of 0.27- $\mu$ m-thick UO<sub>2</sub> scale.

will be referred to comprehensively in the following discussion as a measure of oxidation dynamics.

Apparently, a different energy barrier is involved in each diffusion process. This is demonstrated in Figure 7, where the "A/C" ratio decreases with temperature, indicating that at elevated temperatures the anisotropic diffusion path through (110) is more efficient than the isotropic path. Notably, the anisotropic diffusion path is dominant even at the lower temperatures (120 °C). Apparently, this may be attributed to the fact that for a fine polished surface of the oxide scale, restricted to the elastic growth domain, there is a considerable difference in the relative surface coverage, accounting for the two phenomena. Only a small part of the oxide is covered by defects and boundaries, opposite to continuous coverage of the oxide surface by  $\langle 110 \rangle$  channels in (220). Yet it must be emphasized that for a thick (hundreds of nm) oxide scale, there is no direct route capable of delivering the hopping anion from the oxide-air interface into the interaction proximity of the U cation. The

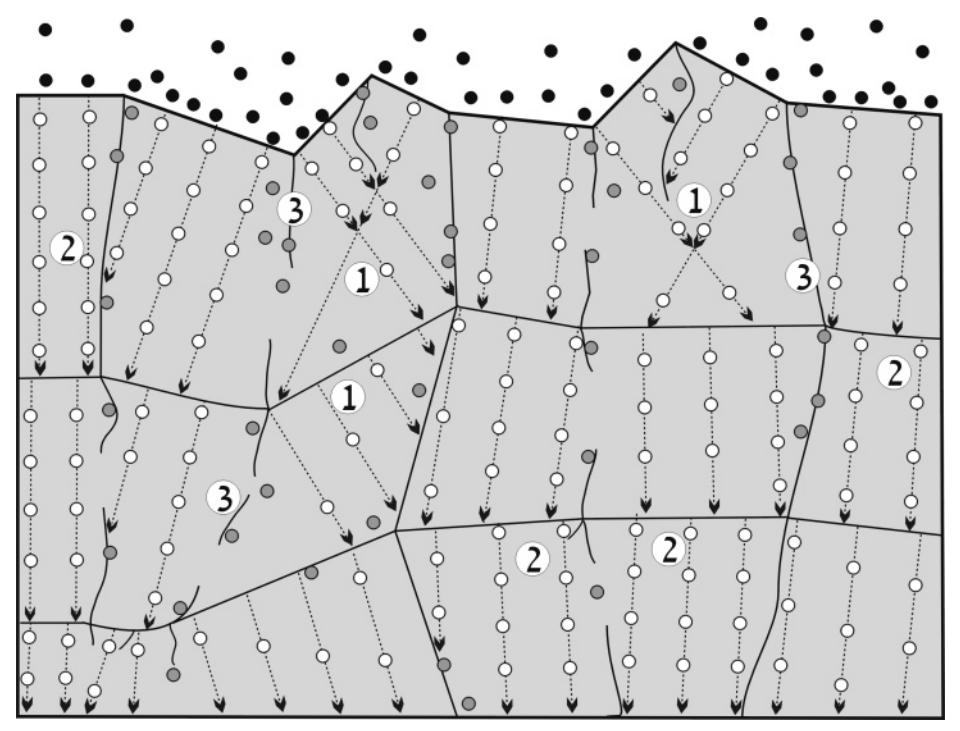


**Figure 8.** Anion transport through adhesive oxide scale. Oxygen anions at the surface (black circles) may reach the oxide—metal interface by anion hopping via the nonperpendicular (110) routes (indicated as "1"-type hopping), by hopping via the perpendicular (110) routes (white circles, "2"-type hopping), or by diffusion via surface defects and oxide—grain boundaries (gray circles, "3"-type anion diffusion).

average grain size of 18 nm defines the mean direct diffusion distance of anions in a single oxide crystal. Hence, anions hop via the  $\langle 110 \rangle$  intergrain-channel net, formed perpendicularly to the upper grain-boundary face, until the subsequent, lower grain boundary is reached. From there, it may instantly proceed via a more recent formed path, toward the next stop. Clearly, the last section of anion transport, before the interaction with cations takes place, undergoes the freshest (220)-channel link. Eventually, an additional link of the (220) in the  $\langle 110 \rangle$  normal to the surface plane is created. Nonetheless, directional oxidation is not a pipeline path process. If a subsequent path is tilted, the anion may diffuse isotropically via a disrupted chain of defects, microcracks, and grain boundaries. It is furthermore assumed that for an oxide grain growing nonperpendicularly (with a majority of its anions paths, tilted accordingly), the concentration of stress-exerted defects is expected to rise. Clearly, this should also effectively disturb anion pipeline hopping in those grains. It is therefore proposed that in the case for which anions hopping via nonperpendicular (110) are disrupted or stopped, anions are expected to diffuse through an isotropic path, and in subsequent argumentation, they are considered as "isotropous anions". Consequently, the higher oxidation rate is achieved if oxide crystallites are oriented in (110), perpendicular to the reacting surface. Seemingly, preferred oxidation buildup is promoted in an oriented crystal surrounding. If the anion fast flow is disturbed (e.g., intercrossing at grain boundaries or coupling to bottleneck paths), the reaction slows down. In such a case, anion flow contributes to the competing reaction path, controlled by isotropic diffusion. This is visualized in Figure 8, where some main anion routes are indicated. The nonperpendicular (110) routes (marked as "1"), are shown to be much less effective in anion delivery than those in the perpendicular (110) (marked as "2"). Diffusion routes via cracks and grain boundaries are marked as "3". We note that an overall lateral stress field gains maximal obstructing power (on (110) pipeline hopping) at orthogonal impact.

D. Stress-Affected Growth Dynamics. Presumably, an unrelieved lateral stress field steadily mounted across the film in the pure elastic growth domain, approaches its maximal strength at the air-oxide interface. The buildup of the stress field is caused by continuous oxidation of the partially oxidized metal grains at the oxide-metal interface and by hyperstoichiometric oxidation of the oxide scale. Since the hyperstoichiometry here is limited, the escalation of the stress field is slow and expansion of the macroscopic elastic domain over thicker scales is facilitated. Yet, the stress field even in the elastic oxide growth domain is usually microscopically relieved by dislocation formation, grain crumbling, and surface rupturing. Indeed, AFM surface profiling revealed an average ~50% rise in root mean square (rms) roughness and the holes/bumps concentration in a 0.33-µm-thick UO<sub>2</sub> scale (with respect to an initial native scale value of  $\sim$ 12 nm). Hence, at a cracking level of locally accumulated lateral stress, defects are created and extended, thus promoting anion diffusion through isotropic and nonperpendicular (110) paths. Dislocation and rupture exerted by a stress field present a maximal enhancing effect on the isotropic anion diffusion at the upper boundary. On the contrary, (110) anion hopping is less disturbed by stress at the metal—oxide boundary. Consequently, the A/C ratio at the inner interface should present a considerably lower value than in the upper part of the UO<sub>2</sub> scale. Indeed, this expected tendency was verified experimentally. A 0.33-µm-oxide scale, grown upon a uranium metal surface, was sputtered and Auger profiled up to a point where the O/U ratio declined to 70% of its initial value (at a depth of  $\sim$ 50% of the initial oxide width). An XRD spectrum of the exposed surface was then taken, revealing a ~20% decrease in the A/C ratio measured previously.

Figure 9 demonstrates the growth dynamics for oxide scales of varying thicknesses, formed at 150 °C, by utilizing the A/C X-ray scattering ratio. The A/C mean ratio diminishes from 0.52 at 0.18- $\mu$ m-thick oxide to a plateau mean value of 0.29 measured for 0.36- $\mu$ m-oxide scale. Afterward, the A/C ratio rises steadily.

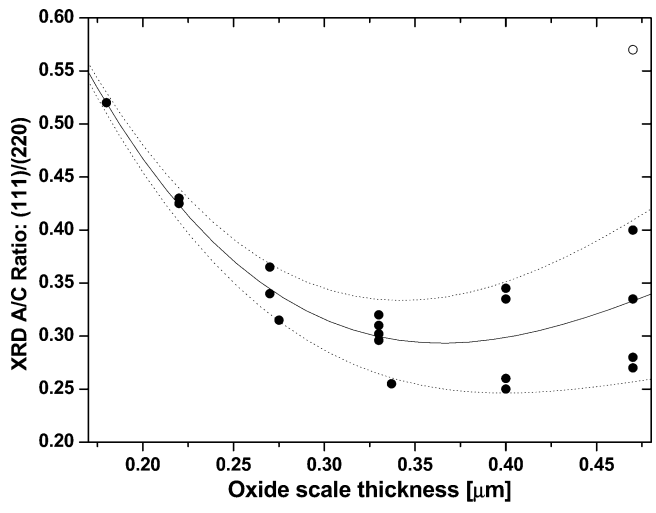


**Figure 9.** XRD A/C-ratio from 20 oxide samples in a 0.18-0.47- $\mu$ m-scale thickness range, obtained at 150 °C. All dots but one (hollow dot) represent fine-polished samples, oxidized during different time periods. Scale thickness was derived from the IR reflectance measurements. Wide error margin domain (shown by dotted lines) includes 95% (second SD) of the points. Solid-line profile presents the calculated (mean) pattern of the A/C values.

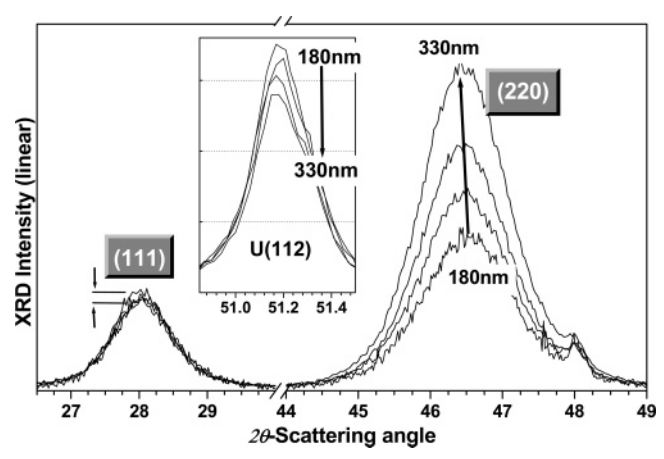


**Figure 10.** Variations in XRD of (111) and (220) of four α-U samples, oxidized (to a different extent) at 150 °C. A correct renormalization<sup>58</sup> of the spectra was obtained by utilizing the estimated oxide scale width for deriving the intensity of the  $\alpha$ -U lines (a renormalized peak of the bulk (112) is displayed in the inset). In the outcome, intensity of the (111) is unchanged (a very small intensity rise can be found for the thickest UO<sub>2</sub>), thus illustrating that in the pure elastic growth domain, there is only a negligible contribution of the isotropic diffusion to the overall rate

This unusual behavior of oxide growth dynamics expresses the principal mechanism of anisotropic versus isotropic diffusionlimited oxidation in a stressed film. As oxide thickness rises, a high rate of hopping anions, anisotropically oriented in  $\langle 110 \rangle$ , is developed. This rate is much higher than any rate obtained due to all other oxidation paths. A climbing stress field, having an overall opposite effect on the anisotropic versus isotropic oxidation paths, gradually changes the kinetic rate constants up to a point, where they are then equalized at the A/C plateau. Eventually, beyond the plateau (Figure 9), the perpendicular rate constant of hopping anions declines below the overall isotropic rate. Yet it should be emphasized that in a pure elastic growth regime, in the applied temperature domain, the rate of isotropic anion diffusion is negligible. Its main impact on the overall oxidation rate is due to the coupling effect on the rate of anisotropic hopping. However, this is not the case for room temperature (RT) oxidation, as demonstrated in the next section. Here, the anisotropic hopping rate is affected mainly due to the direct stress field effect. This point of view (low stress in the elastic growth domain  $\rightarrow$  no rupturing  $\rightarrow$  very low isotropic  $\rightarrow$  high anisotropic rates) is illustrated in Figure 10. It is shown that changes in the A/C ratio of the negative derivative part of the plot in Figure 9 are mostly achieved due to positive changes in (220) scattering intensity alone. There is almost no variation in the intensity of the isotropic path, reflected in the (111) diffraction strength. It is therefore presumed that almost all of the (111) displayed intensity had already been gained due to initial surface roughness and anion isotropic diffusion at RT, before high-temperature oxidation took place (see next section).

While cracking and rupturing exhibit a very limited effect on the isotropic diffusion rate in the pure elastic domain of the oxide scale (less than 0.3  $\mu$ m width), they have an avalanche impact afterward. When critical anion concentration at the oxide-metal interface is breached, the developing stress inflicts cracks, at which point the anion diffusion rate becomes a nonlimiting factor and oxide spall-off occurs. This is shown in Figure 11, which presents FTIR spectra and SEM pictures of an adhesive oxide scale grown during 30 h of oxidation at 130 °C up to a breakaway point. Rupturing and cracking of the oxide taken by SEM are shown in parts A and B of Figure 11. FTIR reflectance presented in part C of Figure 11 displays a complex multiscale interference spectrum. The spectrum is a combination of reflectivities from regions with different oxide contents. Hence, our previously postulated assumption is deductively confirmed by FTIR microscopy, as 0.5- $\mu$ m adhesive oxide scale cover shrinks gradually in favor of the growing portion of islandlike  $2-3-\mu$ m-thick oxide "bumps". Notably, in this transitional post-elastic oxidation regime, our pinpointing A/Cratio grew to 0.64.

**E. Other Dynamic-Affecting Factors.** A noticeable feature in Figure 9 is the highly disperse nature of the A/C ratio. For an oxide width at a breakaway limit, the dispersion attains an extensive  $\pm 30\%$  spread in its second standard deviation. A less substantial spread is achieved at lower thickness. This reproducibility issue in the oxide growth expresses the embodied multiparameter mechanism, affecting the isotropic vs anisotropic rate ratio. Large experimental error margins are mainly caused by the following:

- 1. Variation in the RT Exposure Time of the Sample, before Oxidation. As described, at the initial oxidation stage, perfect perpendicular  $\langle 110 \rangle$  routes are expected to form. Evidently, the extent of anisotropy in this early stage is an important factor in the forthcoming oxidation kinetics. At RT exposure, the isotropic/anisotropic diffusion rate ratio is higher than that obtained at elevated temperatures. Thus, long exposure at RT enlarges the extent of isotropous routes, thus diminishing the anisotropicy of the thin scale. Therefore, anion hopping in the postcoming high-temperature oxidation is slowed. This enlarges the derived A/C ratio effectively.
- 2. Sensitivity to the Surface Roughness. As expressed above, the A/C ratio and the overall oxidation rate are roughness sensitive. A rough surface presents stronger scattering from the projected (1,1,1) and is oxidized at much slower rates than the fine polished one. The difference in the A/C ratio was verified by XRD of two 0.27- $\mu$ m-thick UO<sub>2</sub> samples (see in Figure 12A), distinct only by the amount of initial roughness. The difference in oxidation rate was verified by FTIR reflectance measurements of two uranium samples varying only in their initial roughness. Both samples were oxidized at 140 °C for an equal time period. The measured variation in oxide scale thickness between these

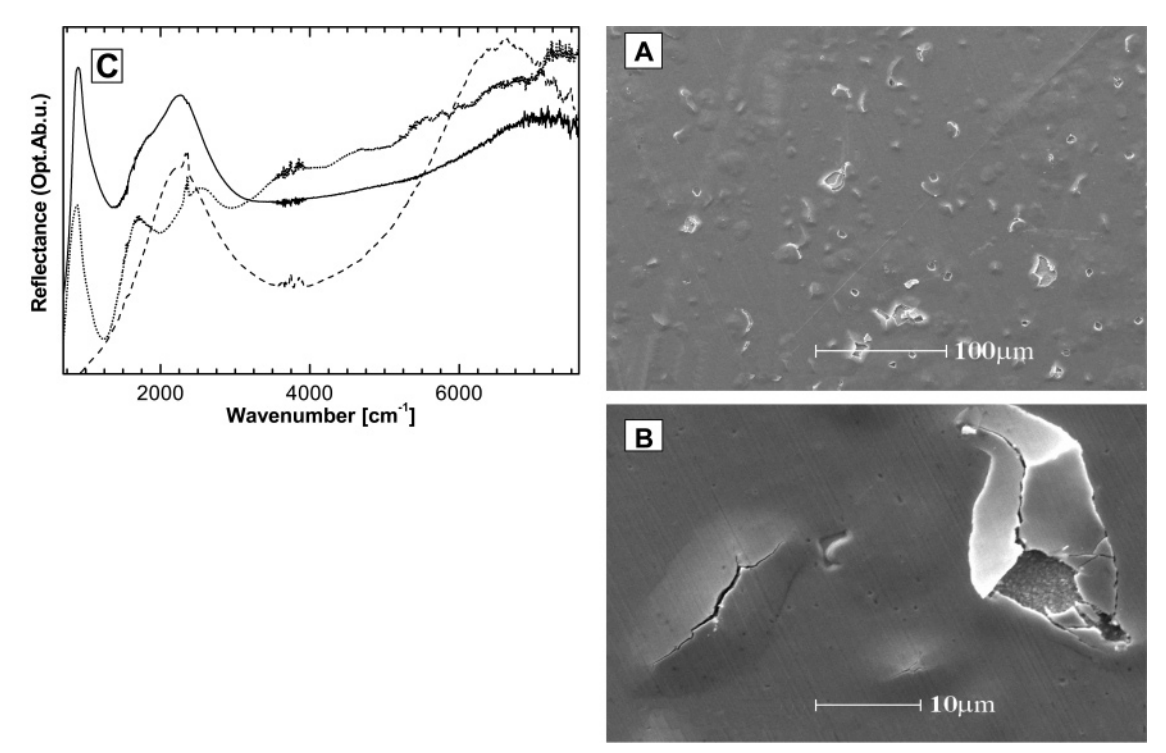
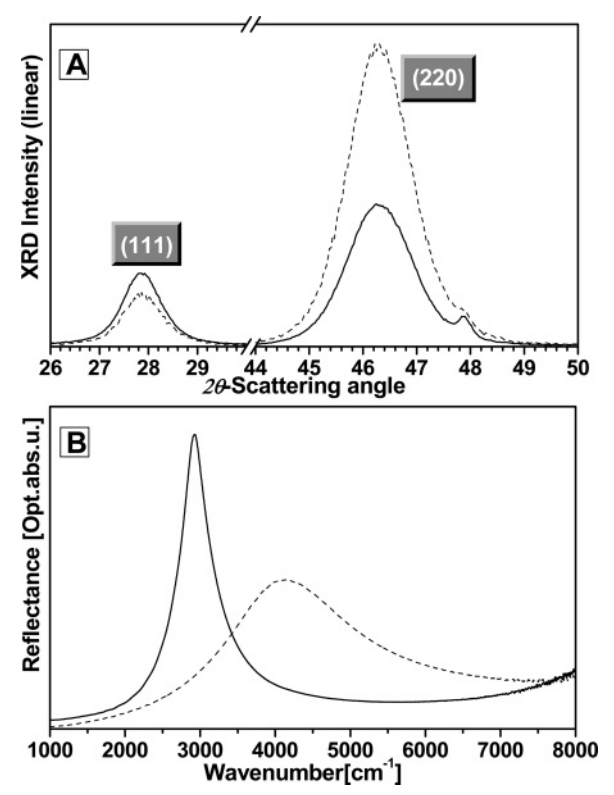
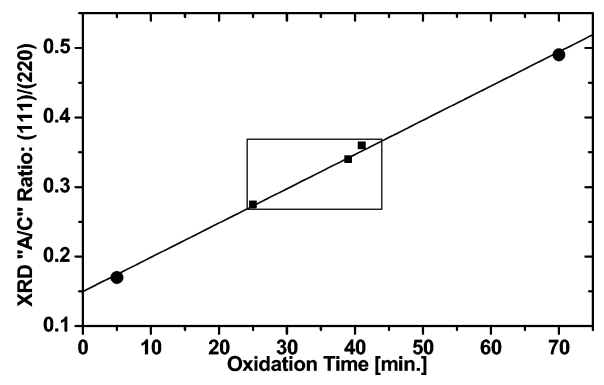


Figure 11. Rupturing and cracking of the oxide scale. The presented oxide scale was obtained at 130 °C (30 h). In A and B, SEM photos are shown: (A) Initial stages of cracking in a stressed, postelastic  $\sim$ 0.5- $\mu$ m-thick UO<sub>2</sub> scale with "bumps". (B) Cracked,  $\sim$ 3- $\mu$ m-thick oxide "bump". Oxide contents in the lateral/bumplike regions described in A and B are revealed by the reflectance FTIR microscopy in C. In C, lateral, bumpless scale of the UO<sub>2</sub> (dashed line) and bump-rich (dotted line) regions are revealed from their basically different interference patterns. A complementary, macroscopic reflectance (solid line) accounts for the spectroscopic features acquired from both sites.



**Figure 12.** Roughness-affected oxidation. (A) Comparison between XRD spectra of (111) and (220) of oxide surface with initial rms roughness of 10 nm (dotted line) and > 30 nm (solid line). Here obtained for 0.27- $\mu$ m scales oxidized at 160 °C. (B) Comparison between FTIR reflectance obtained for oxidized uranium samples, polished either by fine 1  $\mu$ m diamond paste (solid line) or by rough 1 000- mesh polishing paper (dotted line). Both samples were oxidized for 7 h at 140 °C. Reflectance interference peaks indicate 0.41- and 0.27- $\mu$ m-thick oxide scales for the fine and rough polished samples, respectively.



**Figure 13.** Linear time dependence of the A/C-ratio. A/C-ratio of five samples of a 0.27- $\mu$ m-thick  $UO_2$  scale obtained at 160 °C. The spread in the three samples in a central part of a graph (squares) illustrate the effect of a multiparameter dependency in isotropic vs anisotropic oxidation. The two far-most points (large circles) were obtained for samples of a minimal preoxidation time (left-most point) and of a poorly polished surface (right-most point).

samples was  $\sim$ 50% (0.27 and 0.41  $\mu m$  for the rough and the fine-polished samples, respectively), as can be deduced from the results displayed in Figure 12B. This evokes  $\sim$ 2.5 times higher oxidation rate for a fine-polished sample with respect to the rough-polished one.

- 3. Complex Oxidation Behavior Instigated by Deviations in Residual Humidity. A detailed description of the effect is beyond the scope of this work. Yet, evidently one should account for differences in the adsorption rate of  $H_2O$  molecules on cracks, defects, and the exposed (220).
- **4.** Variations in Orientation of the Metal Planes. Changes in concentration of the lateral reactive  $\alpha$ -U planes may affect the oxidation rates in a way associated with a preferred orientation (see notes in Section A).

It should be pointed out that although different in origin, the outcome of all the aforementioned "error"-exerting reasons affects oxidation rates explicitly by controlling the coupling of principal isotropic diffusion vs perpendicular hopping oxidation paths. This is readily demonstrated by the explicit time dependence of the A/C ratio in Figure 13, where samples of 0.27- $\mu$ m-thick  $UO_2$  scale were oxidized at 160 °C. Although the samples exhibited deviation in the overall oxidation rate, a straightforward correlation in oxidation time vs A/C ratio was obtained. Here, the three central points in the graph present a "natural" error spread, exerted by the reproducibility issues discussed above. The two most remote points are caused by an intentional enhancement of the aforementioned factors, 1' (shorter preheating exposure time) and 2' (greater surface roughness).

### Conclusions

The essential part of the intrinsic stress field effect in the diffusion-limited oxidation dynamics of \alpha-U was discussed in a frame of the (110) anion hopping, postulated in the 2:2:2 clustering model. In the elastic growth domain, the macroscopic stress field follows lateral anisotropy. On the basis of X-ray monitoring of  $\Delta(2\theta)$  in (220), a 6.5-GPa lateral stress field was estimated. Structural considerations evoke the growth of UO<sub>2</sub> (220). When combined with kinetically enhanced anion hopping, (110) is utilized as a principal propagation direction for the oxide growth. In the pure elastic growth domain and at higher temperatures (above 120 °C), dynamic hindrance of anion hoping is attributed entirely to the mounting lateral stress. The competing anion diffusion via cracks and grain boundaries is limited to the postelastic (paraplastic) oxidation. In the elastic domain ( $\geq 0.35 \,\mu \text{m}$  range), isotropic diffusion affects oxidation indirectly, mainly by disturbing the strong anion hopping flow. At RT or low temperatures (below 100 °C), the hindering isotropic diffusion effect is far more pronounced, and it obscures pipeline hopping at initial oxidation stages. Roughness presents another hindering factor in the description of anisotropic oxidation dynamics. This qualitative description of α-U oxidation in the presence of a planar stress field still requires a rigorous mathematical formulation in order to obtain a quantitative fitting of the kinetic data set.

The polarized reflectance monitoring technique, utilized for monitoring of the oxidation process is presented.

# Appendix A

**Dielectric Modelization.** Equation A1 describes a factorized form of the Lorenzian shaped single-mode dielectric response,  $^{60}$  utilized here for UO<sub>2</sub> simulation. Here, we exploit the fact that the model allows for different decay mechanisms via  $\gamma_{TO}$  and  $\gamma_{LO}$ , to be explicitly introduced for the transverse and longitudinal phonon vibrations,  $\nu_{TO}$  and  $\nu_{LO}$ , respectively. Selected dielectric parameters are  $\nu_{TO}=286~{\rm cm}^{-1},~\nu_{LO}=574~{\rm cm}^{-1},~\gamma_{TO}=30~{\rm cm}^{-1},~\gamma_{LO}=35~{\rm cm}^{-1},~{\rm and}~\epsilon_{\infty}=5.35.$  They are well fitted to the measured reflection (this includes FIR measurements not shown here) and to the published  $^{12,61}$  data for UO<sub>2</sub>.

$$\epsilon^{B}(\nu) = \epsilon_{\infty} \frac{\nu^{2} + i\gamma_{LO}\nu - \nu_{LO}^{2}}{\nu^{2} + i\gamma_{TO}\nu - \nu_{TO}^{2}}$$
(A1)

Two-scale setup was utilized for a correct description of  $UO_2$  grown upon U. The inner one embodies complex media interface, calculated in accord with the Bruggeman effective media approach<sup>62</sup> (EMA). The concept was to simulate a gradual

shrinkage in the oxide content, accompanied by an elevated concentration of metal inclusions. The assumed topology in Bruggeman EMA theory is of a random mixture of matrix substance and inclusions. Both inclusions and matrix are represented by spherical particles, yielding eq A2,

$$\epsilon_{\rm Br} = (1/4)[\zeta \pm \sqrt{\zeta^2 + 8\epsilon_{\rm UO}\epsilon_{\rm U}}]$$

$$\zeta = (2 - 3f)\epsilon_{\rm UO} + (3f - 1)\epsilon_{\rm U}$$
(A2)

where  $\epsilon_{\rm Br}$  represents composite media,  $\epsilon_{\rm U}$  stands for the dielectric response of the metal, calculated by applying the Kramers–Kroning transform, and  $\epsilon_{\rm UO}$  describes the dioxide, as shown above. Volume fraction of inclusions is given by f. The  $\pm$  sign in the root-square equation is chosen in accord with  ${\rm Im}\{\epsilon_{\rm Br}\} \geq 0$  criteria complement. This scheme was introduced into the inner 50–70 nm oxide–metal interface.

**N-Scale Setup Calculation.** In general, for a multiscale system, Fresnel reflectance is simulated according to eq A3, where j and k are the indexes of two sequential interfaces. The phase shift  $\delta_{j,k}$  in eq A4, is proportional to thickness  $d_{j,k}$ . The reflectance  $r_j$  is calculated in eq A5 for P and S polarizations. Complex, angle-dependent dielectric function,  $\exp(v,\theta)$ , is defined in eq A6. Computation of an overall reflectance r for an n-scale setup initiates from the bottom and gradually converges by recursive collapsing of successive reflectancies:  $r = \{r_1...\{r_{n-1} \leftarrow r_{n-1} \times r_n\}\}$ . Eventually, reflection R is given by  $-rr^*$ .

$$r_{j,k} = \frac{r_j + r_k \exp(i2\delta_{j,k})}{1 + r_k r_i \exp(i2\delta_{j,k})}$$
(A3)

$$\delta_{i,k}^{\rm iso}(\nu,\theta) = 2\pi d_{i,k} \sqrt{\epsilon_i(\nu) - \sin^2(\theta)} \nu \tag{A4}$$

$$r^{p}_{j} = \frac{\epsilon_{j}(\nu) \operatorname{eps}_{j+1}(\nu, \theta) - \epsilon_{j+1}(\nu) \operatorname{eps}_{j}(\nu, \theta)}{\epsilon_{j+1}(\nu) \operatorname{eps}_{i}(\nu, \theta) + \epsilon_{j}(\nu) \operatorname{eps}_{j+1}(\nu, \theta)}$$
(A5a)

$$r^{s}_{j} = \frac{\operatorname{eps}_{j}(\nu, \theta) - \operatorname{eps}_{j+1}(\nu, \theta)}{\operatorname{eps}_{j}(\nu, \theta) + \operatorname{eps}_{j+1}(\nu, \theta)}$$
(A5b)

$$\operatorname{eps}_{i}(\nu,\theta) \equiv \sqrt{\epsilon_{i}(\nu) - \sin^{2}(\theta)}$$
 (A6)

## **References and Notes**

- Hayward, P. J.; Evans, D. G.; Taylor, P.; George, I. M.; Duclos, A. M. J. Nucl. Mater. 1992, 187, 215.
- (2) McGillivray, G. W.; Geeson, D. A.; Greenwood, R. C. J. Nucl. Mater. 1994, 208, 81.
  - (3) Haschke, J. M. J. Alloys Compd. 1998, 278, 149.
  - (4) McEachern, R. J.; Taylor, P. J. Nucl. Mater. 1998, 254, 87.
- (5) Manner, W. L.; Lloyd, J. A.; M. Paffett, T. J. Nucl. Mater. 1999, 275, 37.
- (6) Haschke, J. M.; Allen, T. H.; Morales, L. A. J. Alloys Compd. 2001, 314, 78.
  - (7) Stultz, J.; Paffett, M. T.; Joyce, S. A. J. Phys. Chem. B 2004, 108, 362.
- (8) Uranium Dioxide: Properties and Nuclear Applications; Naval Reactors Group, Division Of Reactor Developments, USAEC; J. Belle, Ed.; U.S. Government Printing Office: Washington, DC, 1961.
- (9) Allen, G. C.; Crofts, J. A.; Griffiths, A. J. J. Nucl. Mater. 1976, 62, 273.
- (10) Bera, S.; Narasimhan, S. V.; Sali, S. K.; Sampath, S.; Venugopal, V. J. Nucl. Mater. 1998, 255, 26.
- (11) Senanayake, S. D.; Rousseau, R.; Colegrave, D.; Idriss, H. J. Nucl. Mater. 2005, 342, 179.
  - (12) Schoenes, J. Phys. Rep. 1980, 63 (6), 301.
  - (13) Begun, G. M.; Haire, R. G. J. Less-Common Met. 1990, 162, 129.
  - (14) Fromhold, A. T. J. Chem. Phys. 1982, 76 (8), 4260.
  - (15) Catlow, C. R. A. Proc. R. Soc. London, Ser. A 1977, 353, 533.

- (16) Tsuji, T.; Matsui, T.; Abe, M.; Naito, K. J. Nucl. Mater. 1989, 168, 151.
- (17) Bleaney, B.; Llewellyn, P. M.; Jones, D. A. Proc. Phys. Soc., London, Ser. B 1956, 69, 858.
  - (18) Willis, B. T. M. Proc. Br. Ceram. Soc. 1964, 1, 9.
- (19) Willis, B. T. M. J. Phys. Radium 1964, 25, 431.
- (20) Baker, J. M.; Davies, E. R.; Hurrell, J. P. Proc. Phys. Soc. A 1968, 308, 403.
- (21) Cheetham, A. K.; Fender, B. E. F.; Cooper, M. J. J. Phys. C: Solid State Phys. 1971, 4, 3107.
  - (22) Catlow, C. R. A. J. Phys. C: Solid State Phys. 1973, 6, 164.
- (23) Catlow, C. R. A. A. Lidiard, B. In *Thermodynamics of Nuclear materials*; International Atomic Energy Authority: Vienna, 1975; Vol. II, pp 27–43.
  - (24) Willis, B. T. M. Acta Crystallogr. 1978, 34, 88.
- (25) Allen, G. C.; Tempest, P. A. J. Chem. Soc., Dalton Trans. 1982, 2169.
- (26) Allen, G. C.; Tempest, P. A. J. Chem. Soc., Dalton Trans. 1983, 2673.
- (27) The 2:2:2 cluster was named after two  $O^{2-}$  interstitials along  $\langle 110 \rangle$ , two  $O^{2-}$  interstitials along  $\langle 111 \rangle$ , and two vacancies in the oxygen lattice.
  - (28) Cabrera, N.; Mott, N. F. *Rep. Prog. Phys.* **1949**, *12*, 163.
  - (29) Atkinson, A. Rev. Mod. Phys. 1985, 57 (2), 437.
  - (30) Grimes, J. H.; Morris, J. R. AWRE Report No. 0-68/65, 1965.
  - (31) Ritchie, A. G. J. Nucl. Mater. 1984, 120, 143.
  - (32) Ritchie, A. G. J. Less. Common Met. 1984, 98, 193.
  - (33) Colmenares, C. A. Prog. Solid State Chem. 1984, 15, 257
- (34) Leibowitz, L.; Schnizlein, J. G.; Bingle, J. D.; Vogel, R. C. *J. Electrochem. Soc.* **1961**, *108* (12), 1155.
  - (35) Hou, P. Y.; Stringer, J. Acta Metall. Mater. 1991, 39 (5), 841.
- (36) Although the presence of some insignificant inherent stress could not be excluded entirely in  $\alpha\textsc{-U}$ , the possible effect of such a microfield on the forthcoming oxidation dynamics was ruled out in this study. This could be assured following stress relief thermal treatment tests, run on reference  $\alpha\textsc{-U}$  samples. The annealed (at 350 °C for 4 h) samples were tested upon oxidation against the untreated samples. No difference (in the annealed versus the untreated samples) in any of the discussed oxidation phenomena could be spotted.
  - (37) Kliewer, K. L.; Fuchs, R. Phys. Rev. 1966, 150 (2), 573.
- (38) Kliewer, K. L.; Fuchs, R.; Pardee, W. J. Phys. Rev. 1966, 150 (2), 589.
  - (39) Mochizuki, S. Phys. Status Solidi B 1985, 128, 23.
- (40) Balkanski, M. Photon—Phonon Interactions in Solids. In *Optical Properties in Solids*; Abeles, F., Ed.; North Holland Publishing Co.: Amsterdam, 1972; Chapter 8.
- (41) Inadequate fit was due to two main reasons: (1) Rietvield treats all components as a homogeneous mixture. This assumption is a source of major errors in our case. Here, a correct scheme should include a thin element scale built over a thick (infinite) element scale, with a sizable interface, consisting of both components, presented in between. (2) A

- noncubic, 2:2:2 superstructure has a substantially lower symmetry than the one attributed to the  $O_n^5$  space group of cubic  $UO_2$ . This would introduce a major issue in fine reconstruction of oxide line-positions, intensity ratios, and line shapes. Strain at specific directions, if not encoded correctly in Rietvield formalism, might further lower the quality of the fit.
- (42) Card # 75-0134 (Calc.), International Center for Diffraction Data (ICDD), 12 Campus Boulevard, Newtown Square, PA, 2003.
- (43) Card # 74-0413 (Calc.), International Center for Diffraction Data (ICDD), 12 Campus Boulevard, Newtown Square, PA, 2003.
- (44) Card # 76-1118 (Calc.), International Center for Diffraction Data (ICDD), 12 Campus Boulevard, Newtown Square, PA, 2003.
- (45) Card # 24-0748 (Calc.), International Center for Diffraction Data (ICDD), 12 Campus Boulevard, Newtown Square, PA, 2003.
- (46) Yashima, M.; Hoshina, T.; Ishimura, D.; Kobayashi, S.; Nakamura, W.; Tsurumi, T.; Wada, S. *J. Appl. Phys.* **2005**, *98*, 14313.
  - (47) Mamantov, E.; Egami, T. J. Phys. Chem. Sol. 2000, 61, 1345.
- (48) Zhang, F.; Chan, S. W.; Spanier, J. E.; Apak, E.; Jin, Q.; Robinson, R. D.; Herman, I. Appl. Phys. Lett. 2002, 80 (17), 127.
- (49) Card # 72-0125 (Calc.), International Center for Diffraction Data (ICDD), 12 Campus Boulevard, Newtown Square, PA, 2003.
- (50) Card # 15-0004, International Center for Diffraction Data (ICDD), 12 Campus Boulevard, Newtown Square, PA, 2003.
- (51) Card # 74-2432 (Calc.), International Center for Diffraction Data (ICDD), 12 Campus Boulevard, Newtown Square, PA, 2003.
- (52) Cullity, B. D. *Elements of X-ray Diffraction*, 2nd ed.; Addison-Wesley: Reading, MA, 1978; Chapter 9.
- (53) Kimmel, G.; Dayan, D.; Frank, D. A.; Landay, A. IAEC Annual Rep., 1996; pp 28–56.
- (54) Yamada, K.; Yamanaka, S.; Nakagawa, T.; Uno, M.; Katsura, M. J. Nucl. Mater. **1997**, 247, 289.
- (55) Elastic constants of single crystals. In CRC Handbook of Chemistry and Physics; CRC: Boca Raton, FL, 2003.
- (56) Thermal and Physical Properties of Pure Metals. In CRC Handbook of Chemistry and Physics; CRC: Boca Raton, FL, 2003.
- (57) Uranium Dioxide: Properties and Nuclear Applications; Naval Reactors Group, Division Of Reactor Developments, USAEC; J. Belle, Ed.; U.S. Government Printing Office: Washington, DC, 1961; pp 192–194.
- (58) We note that the spectra presented in Figure 10 were derived by autonormalization of U(112) intensities according to the Beer–Lambert relation, utilized for an oxide film of known X-ray absorption (derived by density adaptation of published<sup>59</sup> extinction coefficient of U) and thickness (calculated from FTIR reflectance).
- (59) Cullity, B. D. *Elements of X-ray Diffraction*, 2nd ed.; Addison-Wesley: Reading, PA, 1978; Appendix 4.
- (60) Kasic, A.; Schubert, M.; Einfeldt, S.; Hommel, D.; Tiwald, T. E. Phys. Rev. B 2000, 62 (11), 7365.
- (61) Thiry, P. A.; Degbomont, A.; Pireaux, J. J.; Caudano, R.; Naegele, J. R.; Rebizant, J.; Spirlet, J. C. J. Less-Common. Met. 1986, 122, 31.
- (62) Sweet, J. N.; Pettit, R. B.; Chamberlain, M. B. Sol. Energy Mater. 1984, 10, 251.